ACS Photonics

pubs.acs.org/journal/apchd5

Article

Wavelength-Division Multiplexing on an Etchless Lithium Niobate Integrated Platform

Yue Yu,[†] Zejie Yu,[†] Zunyue Zhang,[†] Hon Ki Tsang, and Xiankai Sun*

Cite This: *ACS Photonics* 2022, 9, 3253−3259

Read Online

ACCESS | Metrics & More | Article Recommendations

ABSTRACT: Arrayed waveguide gratings (AWGs) are widely used as (de)multiplexers in wavelength-division-multiplexed optical communication systems and as integrated spectrometers in optical sensing and imaging systems. Lithium niobate integrated photonics is a burgeoning field due to many excellent optical properties of lithium niobate and rapid development of wafer processing technologies. Here, we introduced a new strategy of low-loss waveguiding on an etchless lithium niobate integrated platform for realizing high-performance AWGs thereon. We experimentally demonstrated 4-, 8-, and 16-channel AWGs operating in both telecom and near-visible wavelength bands on the etchless lithium-niobate-on-insulator platform. All the channels have insertion losses below 9.1 dB and crosstalks less than −12.8 dB in the designed wavelength bands. With advantages of an ultrawide transparency window and strong electro-optic and nonlinear optical coefficients of lithium niobate, the demonstrated AWGs will find wide applications in on-chip high-capacity optical interconnects, ultrafast bioimaging, LiDAR, and astronomical spectrographs.

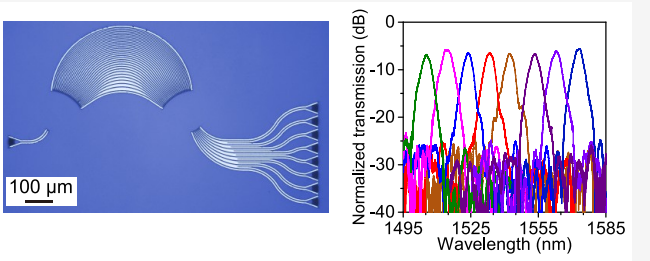

KEYWORDS: *integrated photonics, arrayed waveguide gratings, lithium niobate on insulator, etchless fabrication, optical communication, integrated spectrometers*

INTRODUCTION

Driven by the ever-growing demands for data processing and transmission, optical interconnects with low latency, a high throughput, and a high energy efficiency emerge as a promising technology for constructing high-capacity networks.[1] Arrayed waveguide gratings (AWGs) are a key component for wavelength-division multiplexing (WDM) in high-capacity optical interconnects.[2] They can (de)multiplex channels of several wavelengths into (from) a single optical fiber and are widely used in DWDM telecommunication systems. Due to their low insertion loss, high spectral resolution, and low cost, AWGs have also found other applications including spectroscopy,[3−5] sensing,[6−9] and astronomy.[10−12]

High-performance AWGs have been developed based on various structures with many materials, such as silica-on-Si,[13−15] polymers,[16,17] InP,[18,19] silicon-on-insulator,[20,21] silicon nitride,[22,23] and lithium niobate.[24] Among these materials, lithium niobate is notable for its wide transparency window (400−5000 nm), which supports device operation from the visible to mid-infrared region,[25−28] and its large second-order nonlinearities, which enable their use in high-speed modulators,[29,30] single-photon sources,[31−33] and supercontinuum light emitters.[34] AWGs on lithium-niobate-on-insulator (LNOI) platforms are needed to enable the integration of wavelength multiplexers in high-capacity WDM transmitters and as spectral filters in optical sensing applications. While low-loss waveguides have been demonstrated by etching of lithium niobate,[25,26] attempts at making AWGs on the LNOI platform by conventional etching resulted in an insertion loss of above 25 dB and a phase-error-induced crosstalk of about −10 dB.[24] Here, we introduced a new strategy of low-loss waveguiding and realized high-performance AWGs on an etchless lithium niobate integrated platform by patterning a low-refractive-index material on a high-refractive-index substrate.[35,36] This strategy has been adopted to overcome the difficulties in smooth etching of some difficult-to-etch substrate materials, which enables exploration of their special functionalities on an integrated platform without the need for etching.[37−43] Additionally, devices demonstrated on this platform have shown better thermal stability than those fabricated with the traditional method,[43] which is an advantage for many applications such as optical communication, nonlinear conversion, and quantum photonics.

By fabricating and characterizing 4-, 8-, and 16-channel AWGs with low-loss waveguides, we experimentally demon-

Received: March 18, 2022
Published: September 26, 2022

https://doi.org/10.1021/acsphotonics.2c00437
ACS Photonics 2022, 9, 3253−3259

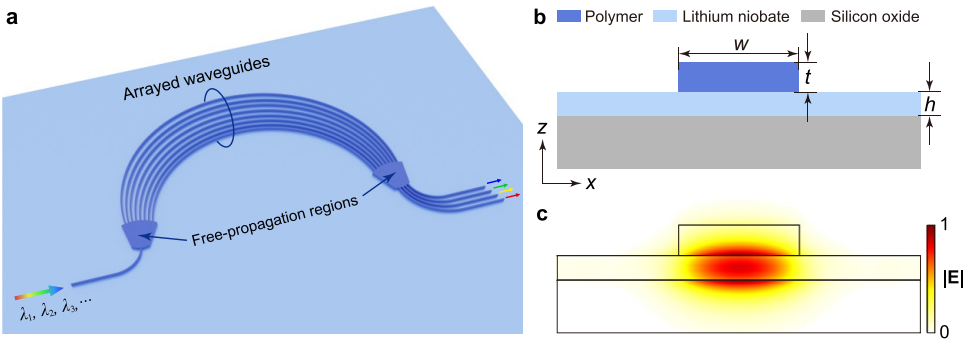

Figure 1. (a) Conceptual illustration of an AWG, which performs the function of wavelength (de)multiplexing by distributing an input light beam with multiple wavelengths to multiple output channels each for a single wavelength or vice versa. A typical AWG includes two free-propagation regions (FPRs) connected by arrayed waveguides between the input and output channels. (b) Cross-sectional view of the waveguide used for constructing the AWG. w and t are the width and thickness of the polymer waveguide, respectively, and h is the thickness of the lithium niobate layer. (c) Modal profile (|**E**| component) of the fundamental TM bound mode supported by the waveguide structure in (b). Although this TM bound mode lies in the TE continuum of the lithium niobate substrate, it can achieve zero theoretical propagation loss for certain combinations of w, t, and h where the BIC condition is satisfied.

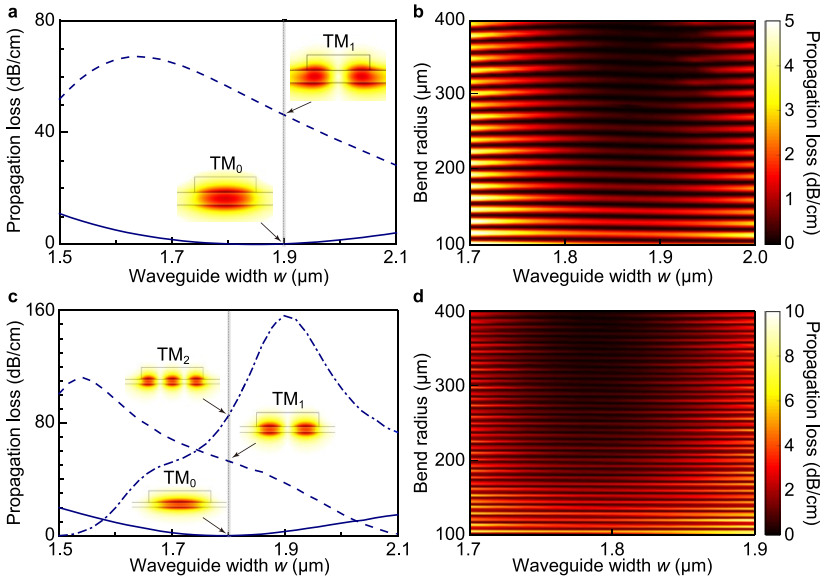

Figure 2. (a) Simulated propagation loss of the TM_0 (solid line) and TM_1 (dashed line) modes of a straight waveguide as a function of the waveguide width w at the wavelength of 1550 nm. The insets show the modal field profiles (|**E**| component) of the two modes at w = 1.9 μm. (b) Simulated propagation loss of the TM_0 mode of a bent waveguide as a function of the waveguide width and bend radius at the wavelength of 1550 nm. (c) Simulated propagation loss of the TM_0 (solid line), TM_1 (dashed line), and TM_2 (dash-dotted line) modes of a straight waveguide as a function of the waveguide width w at the wavelength of 773 nm. The insets show the modal field profiles (|**E**| component) of the three modes at w = 1.8 μm. (d) Simulated propagation loss of the TM_0 mode of a bent waveguide as a function of the waveguide width and bend radius at the wavelength of 773 nm.

strated WDM at both telecom and near-visible wavelengths on an etchless lithium niobate integrated platform. These AWG devices were fabricated with a simple process, which involves only one step of electron-beam lithography without the need for etching the lithium niobate substrate. We characterized the performance of wavelength-division multiplexing by measuring the transmission spectra of the fabricated AWGs. For all the channels, the 8- and 16-channel AWGs working at telecom wavelengths have channel spacings of 9.6 and 3.7 nm, insertion losses of <6.6 and <8.4 dB, and interchannel crosstalks of <−19.3 and <−18.3 dB, respectively; the 4- and 8-channel AWGs working at near-visible wavelengths have channel spacings of 3.3 and 1.8 nm, insertion losses of <4.2 and <9.1 dB, and interchannel crosstalks of <−16.6 and <−12.8 dB, respectively.

DEVICE DESIGN

Figure 1a is a conceptual illustration of the demonstrated AWG. A broadband light beam sent into the input waveguide is diffracted in the first free-propagation region (FPR), which has a shape of the Rowland circle. At the end of the first FPR, the diffracted light reaches the waveguide array and is coupled into the individual waveguides. A constant length difference ΔL is set between adjacent waveguides, which provides a wavelength-dependent optical phase difference such that after propagating through the second FPR, the light of different wavelengths is spatially separated due to interference. By coupling the light of different wavelengths to different output channels, the AWG realizes the function of wavelength demultiplexing. Figure 1b shows the cross section of the designed waveguide structure, which is constructed by a low-

https://doi.org/10.1021/acsphotonics.2c00437
ACS Photonics 2022, 9, 3253−3259

refractive-index polymer waveguide on a high-refractive-index lithium niobate substrate, where w, t, and h are the width of the polymer waveguide, the thickness of the polymer waveguide, and the thickness of the lithium niobate layer, respectively. Figure 1c plots the modal profile (|E| component) of the fundamental TM bound mode supported by the waveguide structure in Figure 1b. In such a waveguide structure, the TM bound mode [Figure 1c] lies in the TE continuum of the lithium niobate substrate, which usually yields energy dissipation of the former to the latter. One can engineer the waveguide geometry such that the TM bound mode turns into a bound state in the continuum (BIC), which has zero theoretical loss to the substrate continuum.[35] This has formed the basis for our experimental demonstration of etchless lithium niobate integrated photonics, achieving a minimal propagation loss of 1.5 (1.8) dB cm^{-1} in waveguides and a maximal intrinsic Q factor of 5.8×10^5 (1.1×10^6) in microcavities in the telecom (near-visible) wavelength band.[36,37]

Here, all the AWGs were designed on the LNOI platform. To facilitate low-loss single-mode operation in the waveguides, wafers with different thicknesses of lithium niobate thin films should be used for different working wavelengths. We chose LNOI wafers with 400- and 150-nm-thick z-cut lithium niobate layers on 2-μm-thick silicon oxide for AWGs working at telecom and near-visible wavelengths, respectively. To obtain low insertion loss, the propagation loss of both the straight and bent waveguides should be minimized simultaneously. In a straight waveguide, the TM bound mode has an attenuation length that is proportional to $w^2/\sin^2(k_x w/2)$, with k_x being the x component of the wave vector of the TE continuous mode which matches that of the TM bound mode.[35] Note that for waveguide width w < 2.1 μm, the waveguide structure for telecom wavelengths can only support the TM bound modes up to the first order (TM_0 and TM_1), and the waveguide structure for near-visible wavelengths can only support the TM bound modes up to the second order (TM_0, TM_1, and TM_2). Figure 2a,c plots the propagation loss of these supported TM modes in a straight waveguide as a function of the waveguide width w at telecom and near-visible wavelengths, respectively. It is straightforward to choose the waveguide widths of 1.9 and 1.8 μm for operation at telecom and near-visible wavelengths, respectively. Under these conditions, the fundamental TM mode turns into a BIC with near-zero propagation loss while all the high-order modes are highly lossy, which effectively supports single-mode operation in the respective waveguide structure. In a bent waveguide, the TM bound mode has a propagation loss depending on both the bend radius and waveguide width.[36,37] Figure 2b,d plots the propagation loss of the fundamental TM mode in a bent waveguide as a function of the waveguide width and bend radius at telecom and near-visible wavelengths, respectively. It is clear that the loss oscillates with a decaying amplitude as the bend radius increases.[35] Since the requirement of a constant phase delay between adjacent arrayed waveguides makes it difficult to select all the bend radii at the exact BIC condition, we designed the bend radii of the arrayed waveguides to be >220 μm, where the upper bound of the propagation loss is 1.1 and 1.4 dB/cm at the wavelengths of 1550 and 773 nm with the waveguide widths of 1.9 and 1.8 μm, respectively. In the designed waveguides, the calculated effective refractive index and group index are 1.745 and 2.211, respectively, at the wavelength of 1550 nm and are 1.677 and 2.083, respectively, at the wavelength of 773 nm. Based on the operating principle of AWGs, for a specific center wavelength λ_0, channel spacing $\Delta\lambda_{ch}$, and operating bandwidth, the design parameters include the number of arrayed waveguides N_{wg}, the waveguide length increment ΔL, and the FPR length L_{FPR}. We used adiabatic tapers between the single-mode waveguides and FPRs to reduce the transition loss. Table 1 lists all the design parameters of the AWGs for both telecom and near-visible wavelengths.

Table 1. Design Parameters of the Demonstrated AWGs

	telecom		near-visible	
parameters	8-channel	16-channel	4-channel	8-channel
h (nm)	400	400	150	150
t (nm)	500	500	400	400
w (μm)	1.9	1.9	1.8	1.8
N_{wg}	32	64	16	32
λ_0 (nm)	1540	1525	773	773
$\Delta\lambda_{ch}$ (nm)	10.0	4.0	3.0	1.8
ΔL (μm)	13.8	17.2	24.0	20.0
L_{FPR} (μm)	145.2	291.2	139.2	278.4

To evaluate the interchannel crosstalks of the AWGs, we simulated the spectra of 4-, 8-, and 16-channel AWGs with 16, 32, and 64 arrayed waveguides by using the dispersion of the arrayed waveguides obtained from Lumerical mode solver. Figure 3a,b plots the output spectra of an 8- and 16-channel AWG at telecom wavelengths, respectively. Figure 3c,d plots the output spectra of a 4- and 8-channel AWG at near-visible wavelengths, respectively. According to these simulated results, at telecom wavelengths, the designed 8- and 16-channel AWGs have channel spacings of 10.0 and 4.0 nm, operating bandwidths of 80.0 and 64.0 nm, and adjacent-channel crosstalks of −18.4 and −17.6 dB, respectively. At near-visible wavelengths, the designed 4- and 8-channel AWGs have channel spacings of 3.0 and 1.8 nm, operating bandwidths of 12.0 and 14.4 nm, and adjacent-channel crosstalks of −16.7 and −17.5 dB, respectively.

EXPERIMENTAL RESULTS

We fabricated the AWG devices on LNOI wafers manufactured by NANOLN. The fabrication procedure is as follows: after wafer cleaning with acetone and isopropanol, a polymer (ZEP520A) was spin-coated on the wafer at 2300 (3300) rpm for 1 min and then prebaked on a hot plate at 180 °C for 3 min, which produced a polymer thin film with ∼500 (∼400) nm thickness. Then, the AWG patterns were defined in the polymer thin film by using a high-resolution electron-beam lithography system (Elionix ELS7800) with a beam current of 500 pA and a dose of 180−220 $\mu C/cm^2$. After the electron-beam exposure, the wafer was developed in ZED-N50 at 0 °C for 1 min, then rinsed in a mixture of methyl isobutyl ketone and isopropanol (9:1) at room temperature for 30 s, and blow-dried. The fabricated devices are quite stable in the ambient environment and do not have noticeable degradation in their performance several years after fabrication.

Figure 4a shows the optical microscope image of a fabricated 8-channel AWG. Grating couplers were utilized to couple light into and out of the device because they not only facilitate power coupling between optical fibers and the chip but also serve as polarizers enabling high-efficiency excitation of the

https://doi.org/10.1021/acsphotonics.2c00437
ACS Photonics 2022, 9, 3253−3259

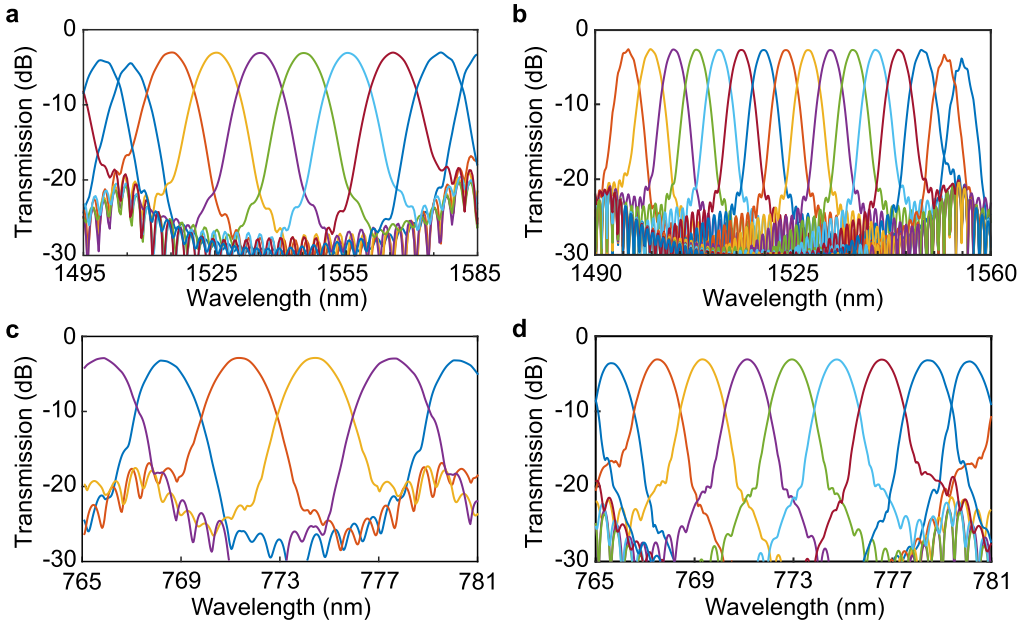

Figure 3. (a,b) Simulated output spectra of an 8-channel (a) and 16-channel (b) AWG working at telecom wavelengths. (c,d) Simulated output spectra of a 4-channel (c) and 8-channel (d) AWG working at near-visible wavelengths.

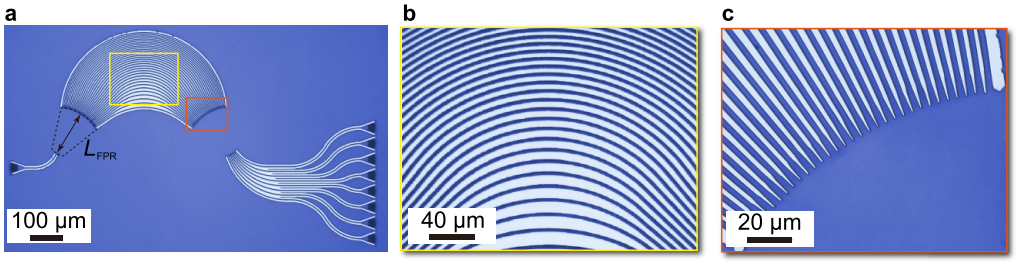

Figure 4. Optical microscope images of a fabricated 8-channel AWG. (a) Overview of the entire device. The two FPRs have the same shape and dimensions, while the left one is indicated by the dashed sector. (b) Close-up of the arrayed waveguides in the region marked by the yellow rectangle in (a). (c) Close-up of the transition region marked by the orange rectangle in (a), where parabolic tapers are used to reduce the insertion loss.

fundamental TM mode in the on-chip waveguides.[35] To calibrate the insertion loss of these grating couplers, control devices with a pair of grating couplers connected by a straight waveguide were also fabricated on the same chip. Figure 4b is a close-up of the arrayed waveguides in the region marked by the yellow rectangle in Figure 4a. Figure 4c is a close-up of the transition region that connects the arrayed waveguides with the FPR, as marked by the orange rectangle in Figure 4a.

The fabricated AWG devices were characterized by spectral measurements of their optical transmission. Light from a tunable semiconductor laser was sent through a fiber polarization controller and then coupled into the device via the input grating coupler. The transmitted light coupled out of each output grating coupler was collected by a photodetector. Figure 5 shows the normalized transmission spectra of all the channels and of the central channel measured from the fabricated four types of AWGs. Note that these transmission spectra were normalized by the transmission of the corresponding control devices. At telecom wavelengths, the 8- and 16-channel AWGs had measured channel spacings of 9.6 and 3.7 nm and operating bandwidths of 76.8 and 59.2 nm, respectively. The measured insertion losses were below 6.6 and 8.4 dB, respectively. The measured crosstalks were below −19.3 and −18.3 dB for adjacent channels and were below −24.1 and −16.5 dB for nonadjacent channels, respectively. The inferior performance of the simulated crosstalks for adjacent channels is attributed mainly to the approximation in our simulation by truncating the optical field in each waveguide at the transition interface, which added extra sidelobes in the output spectra. At near-visible wavelengths, the 4- and 8-channel AWGs had measured channel spacings of 3.3 and 1.8 nm and operating bandwidths of 13.2 and 14.4 nm, respectively. The measured insertion losses were below 4.2 and 9.1 dB, respectively. The measured crosstalks were below −16.6 and −12.8 dB for adjacent channels and were below −24.0 and −17.7 dB for nonadjacent channels, respectively. All the four types of AWG devices had measured channel spacings and operating bandwidths in good agreement with the designed values. The relatively large insertion loss of the fabricated devices is attributed mainly to (1) the transition loss at the interfaces of the FPRs and the arrayed waveguides due to modal mismatch and (2) the propagation loss in the arrayed waveguides. The transition loss can be further reduced by optimizing the transition between the FPRs and the arrayed waveguides by using smaller gaps between the arrayed waveguides. The propagation loss in the arrayed waveguides can be further reduced by using the U-shaped layout for the arrayed waveguides,[44] which share an identical bend radius to

https://doi.org/10.1021/acsphotonics.2c00437
ACS Photonics 2022, 9, 3253−3259

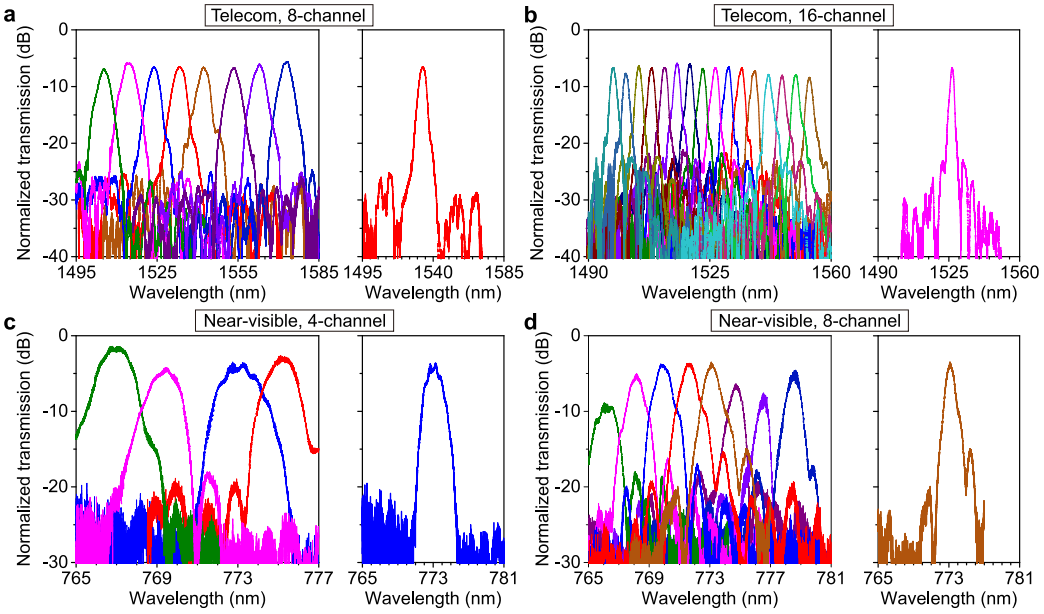

Figure 5. (a) Normalized transmission spectra of all the channels (left) and of the central channel (right) measured from the fabricated 8-channel AWG at telecom wavelengths. (b) Normalized transmission spectra of all the channels (left) and of the central channel (right) measured from the fabricated 16-channel AWG at telecom wavelengths. (c) Normalized transmission spectra of all the channels (left) and of the central channel (right) measured from the fabricated 4-channel AWG at near-visible wavelengths. (d) Normalized transmission spectra of all the channels (left) and of the central channel (right) measured from the fabricated 8-channel AWG at near-visible wavelengths.

facilitate selection of a smaller bend radius satisfying the BIC condition. The propagation loss can also be reduced by improving the fabrication processes such as postbaking to reduce the surface roughness of the waveguides. Additionally, two noticeable sidelobes can be found on both sides of the main peak as shown in some spectra of the central channel. This phenomenon can be attributed to the limited number of arrayed waveguides and the unwanted phase errors in the arrayed waveguides. For example, abrupt changes in waveguide boundaries can cause waveguide effective refractive index variation and thus give rise to considerable phase errors. Therefore, improving the fabrication processes will also help to suppress these sidelobes and reduce the crosstalk.

CONCLUSIONS

We have realized WDM on an etchless lithium niobate integrated photonic platform. We experimentally demonstrated 4-, 8-, and 16-channel AWGs on LNOI wafers operating at both telecom and near-visible wavelengths. The devices were fabricated with a simple etchless fabrication method that does not need etching of lithium niobate. These AWG devices exhibit the best reported performance yet achieved on lithium niobate integrated photonic platforms. At telecom wavelengths, the fabricated 8- and 16-channel AWGs have operating bandwidths of 76.8 and 59.2 nm, insertion losses below 6.6 and 8.4 dB, and adjacent-channel crosstalks below −19.3 and −18.3 dB, respectively. At near-visible wavelengths, the fabricated 4- and 8-channel AWGs have operating bandwidths of 13.2 and 14.4 nm, insertion losses below 4.2 and 9.1 dB, and adjacent-channel crosstalks below −16.6 and −12.8 dB, respectively. The insertion loss and crosstalk can be further reduced by optimizing the transition between the FPRs and the arrayed waveguides and/or by improving the fabrication processes. As a wavelength (de)multiplexer in wavelength-division-multiplexed systems or an integrated spectrometer in imaging and sensing systems, the demonstrated AWGs pave the way for the development of lithium niobate photonic integrated circuits with significantly enhanced operating bandwidths, which may enable new applications in high-capacity telecommunication, high-resolution imaging, and high-speed sensing.

AUTHOR INFORMATION

Corresponding Author

Xiankai Sun − *Department of Electronic Engineering, The Chinese University of Hong Kong, Shatin, Hong Kong SAR, China;* orcid.org/0000-0002-9137-0298; Email: xksun@cuhk.edu.hk

Authors

Yue Yu − *Department of Electronic Engineering, The Chinese University of Hong Kong, Shatin, Hong Kong SAR, China*

Zejie Yu − *Department of Electronic Engineering, The Chinese University of Hong Kong, Shatin, Hong Kong SAR, China;* Present Address: College of Optical Science and Engineering, Zhejiang University, Hangzhou, Zhejiang 310058, China; orcid.org/0000-0002-3067-3965

Zunyue Zhang − *Department of Electronic Engineering, The Chinese University of Hong Kong, Shatin, Hong Kong SAR, China;* orcid.org/0000-0002-1674-3680

Hon Ki Tsang − *Department of Electronic Engineering, The Chinese University of Hong Kong, Shatin, Hong Kong SAR, China;* orcid.org/0000-0003-2777-1537

Complete contact information is available at: https://pubs.acs.org/10.1021/acsphotonics.2c00437

Author Contributions

†Y.Y., Z.Y., and Z.Z. contributed equally to this work.

Funding

This work was funded by the Research Grants Council of Hong Kong (14206318, 14208421) and by Strategic Partnership Award for Research Collaboration offered by The Chinese

https://doi.org/10.1021/acsphotonics.2c00437
ACS Photonics 2022, 9, 3253−3259

University of Hong Kong. Zunyue Zhang would like to thank ITF Talent Hub for funding support.

Notes

The authors declare no competing financial interest.

REFERENCES

(1) Cheng, Q. X.; Bahadori, M.; Glick, M.; Rumley, S.; Bergman, K. Recent advances in optical technologies for data centers: A review. *Optica* **2018**, *5*, 1354−1370.

(2) Smit, M. K.; Van Dam, C. PHASAR-based WDM-devices: Principles, design and applications. *IEEE J. Sel. Top. Quantum Electron.* **1996**, *2*, 236−250.

(3) Ismail, N.; Choo-Smith, L. P.; Wörhoff, K.; Driessen, A.; Baclig, A. C.; Caspers, P. J.; Puppels, G. J.; de Ridder, R. M.; Pollnau, M. Raman spectroscopy with an integrated arrayed-waveguide grating. *Opt. Lett.* **2011**, *36*, 4629−4631.

(4) Cheben, P.; Schmid, J. H.; Delâge, A.; Densmore, A.; Janz, S.; Lamontagne, B.; Lapointe, J.; Post, E.; Waldron, P.; Xu, D. X. A high-resolution silicon-on-insulator arrayed waveguide grating microspectrometer with sub-micrometer aperture waveguides. *Opt. Express* **2007**, *15*, 2299−2306.

(5) Hu, Z.; Glidle, A.; Ironside, C.; Cooper, J. M.; Yin, H. An integrated microspectrometer for localised multiplexing measurements. *Lab Chip* **2015**, *15*, 283−289.

(6) Wang, R.; Vasiliev, A.; Muneeb, M.; Malik, A.; Sprengel, S.; Boehm, G.; Amann, M.-C.; Šimonytė, I.; Vizbaras, A.; Vizbaras, K.; Baets, R.; Roelkens, G. III−V-on-silicon photonic integrated circuits for spectroscopic sensing in the 2−4 μm wavelength range. *Sensors* **2017**, *17*, 1788.

(7) Kodate, K.; Komai, Y. Compact spectroscopic sensor using an arrayed waveguide grating. *J. Opt. A: Pure Appl. Opt.* **2008**, *10*, 044011.

(8) Wu, W.; Liu, X. Fiber Bragg grating sensors interrogation system using arrayed waveguide gratings demultiplexer. *Asia Communications and Photonics Conference and Exhibition, Shanghai, China*, 2009, p. WL27.

(9) Yebo, N. A.; Bogaerts, W.; Hens, Z.; Baets, R. On-chip arrayed waveguide grating interrogated silicon-on-insulator microring resonator-based gas sensor. *IEEE Photonics Technol. Lett.* **2011**, *23*, 1505−1507.

(10) Bland-Hawthorn, J.; Horton, A. Instruments without optics: An integrated photonic spectrograph. *Proc. SPIE* **2006**, *6269*, 62690N.

(11) Jovanovic, N.; Schwab, C.; Cvetojevic, N.; Guyon, O.; Martinache, F. Enhancing stellar spectroscopy with extreme adaptive optics and photonics. *Publ. Astron. Soc. Pac.* **2016**, *128*, 121001.

(12) Stoll, A.; Zhang, Z.; Haynes, R.; Roth, M. High-resolution arrayed-waveguide-gratings in astronomy: Design and fabrication challenges. *Photonics* **2017**, *4*, 30.

(13) Hibino, Y. Recent advances in high-density and large-scale AWG multi/demultiplexers with higher index-contrast silica-based PLCs. *IEEE J. Sel. Top. Quantum Electron.* **2002**, *8*, 1090−1101.

(14) Kohtoku, M. Low-loss compact silica—based AWG using deep ridge waveguide. *Integrated Photonics Research and Applications Conference, San Diego, California, USA*, 2005; p ITuF1.

(15) Kamei, S.; Doi, Y.; Hida, Y.; Inoue, Y.; Suzuki, S.; Okamoto, K. Low-loss and flat/wide-passband CWDM demultiplexer using silica-based AWG with multi-mode output waveguides. *Optical Fiber Communication Conference, Los Angeles, California, USA*, 2004; p TuI2.

(16) Juhari, N.; Yusof, M. F.; Abd Wahid, M. H.; Ismail, N. S. Design of arrayed waveguide grating (AWG) demultiplexer based PMMA for narrow channel spacing. *AIP Conf. Proc.* **2019**, *2203*, 020056.

(17) Yang, B.; Zhu, Y.; Jiao, Y.; Yang, L.; Sheng, Z.; He, S.; Dai, D. Compact arrayed waveguide grating devices based on small SU-8 strip waveguides. *J. Lightwave Technol.* **2011**, *29*, 2009−2014.

(18) Doerr, C. R.; Zhang, L.; Winzer, P. J. Monolithic InP multiwavelength coherent receiver using a chirped arrayed waveguide grating. *J. Lightwave Technol.* **2011**, *29*, 536−541.

(19) Yurt, N.; Rausch, K.; Kost, A. R.; Peyghambarian, N. Design and fabrication of a broadband polarization and temperature insensitive arrayed waveguide grating on InP. *Opt. Express* **2005**, *13*, 5535−5541.

(20) Ye, T.; Fu, Y.; Qiao, L.; Chu, T. Low-crosstalk Si arrayed waveguide grating with parabolic tapers. *Opt. Express* **2014**, *22*, 31899−31906.

(21) Cheung, S.; Su, T. H.; Okamoto, K.; Yoo, S. J. B. Ultra-compact silicon photonic 512 x 512 25 GHz arrayed waveguide grating router. *IEEE J. Sel. Top. Quantum Electron.* **2013**, *20*, 310−316.

(22) Dai, D.; Wang, Z.; Bauters, J. F.; Tien, M. C.; Heck, M. J. R.; Blumenthal, D. J.; Bowers, J. E. Low-loss Si_3N_4 arrayed-waveguide grating (de)multiplexer using nano-core optical waveguides. *Opt. Express* **2011**, *19*, 14130−14136.

(23) Zhang, Z.; Wang, Y.; Tsang, H. K. Ultracompact 40-channel arrayed waveguide grating on silicon nitride platform at 860 nm. *IEEE J. Quantum Electron.* **2020**, *56*, 8400308.

(24) Prost, M.; Liu, G.; Yoo, S. J. B. A compact thin-film lithium niobate platform with arrayed waveguide gratings and MMIs. *Optical Fiber Communications Conference and Exposition, San Diego, California, USA*, 2018; p Tu3A.3.

(25) Desiatov, B.; Shams-Ansari, A.; Zhang, M.; Wang, C.; Lončar, M. Ultra-low-loss integrated visible photonics using thin-film lithium niobate. *Optica* **2019**, *6*, 380−384.

(26) Zhang, M.; Wang, C.; Cheng, R.; Shams-Ansari, A.; Lončar, M. Monolithic ultra-high-Q lithium niobate microring resonator. *Optica* **2017**, *4*, 1536−1537.

(27) Wang, M.; Wu, R.; Lin, J.; Zhang, J.; Fang, Z.; Chai, Z.; Cheng, Y. Chemo-mechanical polish lithography: A pathway to low loss large-scale photonic integration on lithium niobate on insulator. *Quantum Eng.* **2019**, *1*, e9.

(28) Luke, K.; Kharel, P.; Reimer, C.; He, L.; Loncar, M.; Zhang, M. Wafer-scale low-loss lithium niobate photonic integrated circuits. *Opt. Express* **2020**, *28*, 24452−24458.

(29) Wang, C.; Zhang, M.; Chen, X.; Bertrand, M.; Shams-Ansari, A.; Chandrasekhar, S.; Winzer, P.; Lončar, M. Integrated lithium niobate electro-optic modulators operating at CMOS-compatible voltages. *Nature* **2018**, *562*, 101−104.

(30) Wang, C.; Zhang, M.; Stern, B.; Lipson, M.; Lončar, M. Nanophotonic lithium niobate electro-optic modulators. *Opt. Express* **2018**, *26*, 1547−1555.

(31) Montaut, N.; Sansoni, L.; Meyer-Scott, E.; Ricken, R.; Quiring, V.; Herrmann, H.; Silberhorn, C. High-efficiency plug-and-play source of heralded single photons. *Phys. Rev. Appl.* **2017**, *8*, 024021.

(32) Xiang, T.; Li, Y.; Zheng, Y.; Chen, X. Multiple-DWDM-channel heralded single-photon source based on a periodically poled lithium niobate waveguide. *Opt. Express* **2017**, *25*, 12493−12498.

(33) Main, P.; Mosley, P. J.; Ding, W.; Zhang, L.; Gorbach, A. V. Hybrid microfiber−lithium-niobate nanowaveguide structures as high-purity heralded single-photon sources. *Phys. Rev. A* **2016**, *94*, 063844.

(34) Lu, J.; Surya, J. B.; Liu, X.; Xu, Y.; Tang, H. X. Octave-spanning supercontinuum generation in nanoscale lithium niobate waveguides. *Opt. Lett.* **2019**, *44*, 1492−1495.

(35) Zou, C.-L.; Cui, J.-M.; Sun, F.-W.; Xiong, X.; Zou, X.-B.; Han, Z.-F.; Guo, G.-C. Guiding light through optical bound states in the continuum for ultrahigh-Q microresonators. *Laser Photonics Rev.* **2015**, *9*, 114−119.

(36) Yu, Z.; Xi, X.; Ma, J.; Tsang, H. K.; Zou, C.-L.; Sun, X. Photonic integrated circuits with bound states in the continuum. *Optica* **2019**, *6*, 1342−1348.

(37) Yu, Y.; Yu, Z.; Wang, L.; Sun, X. Ultralow-loss etchless lithium niobate integrated photonics at near-visible wavelengths. *Adv. Opt. Mater.* **2021**, *9*, 2100060.

(38) Yu, Z.; Wang, Y.; Sun, B.; Tong, Y.; Xu, J.-B.; Tsang, H. K.; Sun, X. Hybrid 2D-material photonics with bound states in the continuum. *Adv. Opt. Mater.* **2019**, *7*, 1901306.

https://doi.org/10.1021/acsphotonics.2c00437
ACS Photonics 2022, 9, 3253−3259

(39) Yu, Z.; Tong, Y.; Tsang, H. K.; Sun, X. High-dimensional communication on etchless lithium niobate platform with photonic bound states in the continuum. *Nat. Commun.* **2020**, *11*, 2602.
(40) Yu, Z.; Sun, X. Acousto-optic modulation of photonic bound state in the continuum. *Light Sci. Appl.* **2020**, *9*, 1.
(41) Yu, Y.; Wang, L.; Sun, X. Demonstration of on-chip gigahertz acousto-optic modulation at near-visible wavelengths. *Nanophotonics* **2021**, *10*, 4323−4329.
(42) Yu, Z.; Sun, X. Gigahertz acousto-optic modulation and frequency shifting on etchless lithium niobate integrated platform. *ACS Photonics* **2021**, *8*, 798−803.
(43) Ye, F.; Yu, Y.; Xi, X.; Sun, X. Second-harmonic generation in etchless lithium niobate nanophotonic waveguides with bound states in the continuum. *Laser Photonics Rev.* **2022**, *16*, 2100429.
(44) Martens, D.; Subramanian, A. Z.; Pathak, S.; Vanslembrouck, M.; Bienstman, P.; Bogaerts, W.; Baets, R. G. Compact silicon nitride arrayed waveguide gratings for very near-infrared wavelengths. *IEEE Photonics Technol. Lett.* **2015**, *27*, 137−140.

https://doi.org/10.1021/acsphotonics.2c00437
ACS Photonics 2022, 9, 3253−3259